Far infrared observations of the southern Galactic star forming complex around IRAS 09002-4732

S.K. Ghosh[1], **B. Mookerjea**[1], **T.N. Rengarajan**[1], **S.N. Tandon**[2], **and R.P. Verma**[1]

[1] Tata Institute of Fundamental Research, Homi Bhabha Road, Mumbai (Bombay) 400 005, India
[2] Inter-University Centre for Astronomy & Astrophysics, Ganeshkhind, Pune 411 007, India

Abstract. The Galactic star forming region in the southern sky, associated with IRAS 09002-4732 has been mapped simultaneously in two far infrared bands (λ_{eff} = 148 & 209 μm), with $\sim 1'$ angular resolution. Fifteen sources, including IRAS 08583-4719, 08589-4714, 09002-4732 and 09014-4736 have been detected, some of which are well resolved. Taking advantage of similar beams in the two bands, a reliable dust temperature [T(148/209)] map has been obtained, which detects colder dust (< 30 K) in this region. The HIRES processed IRAS maps at 12, 25, 60 and 100 μm, have also been used for comparison. The optical depth maps, τ_{200} and τ_{100}, generated from these far-IR data quantify the spatial distribution of the dust. The diffuse emission from this entire region has been found to be 35% of the total FIR luminosity. The slope of the IMF in the mass range 4–16 $M_\odot$ has been estimated to be $-1.25^{+0.75}_{-0.65}$ for this star forming complex.

Radiative transfer models in spherical geometry have been explored to fit available observations of the 4 IRAS sources and extract various physical parameters for corresponding dust-gas clouds. Whereas a constant (r^0) radial density distribution is favoured in IRAS 08583-4719, 08589-4714 and 09002-4732, the r^{-1} law is inferred for IRAS 09014-4736. The dust composition is found to be similar (Silicate dominated) in all four IRAS sources modelled. The luminosity per unit mass is found to be in the narrow range of $44 - 81$ $L_\odot/M_\odot$ for these star forming regions.

Key words: ISM: dust, extinction – ISM: H II regions – ISM: individual objects: IRAS 09002-4732 – infrared: ISM: continuum

1. Introduction

The study of far infrared (FIR) emission from the relatively denser regions of the Galactic interstellar medium (ISM) is useful for understanding the star formation process. High spatial resolution mapping of Galactic molecular clouds in the FIR

continuum (in ≥ 2 bands) provides direct information about the physical conditions (e.g. total luminosity, dust distribution, dust temperature etc.) of the region. For a constant gas-to-dust ratio, the dust optical depth traces matter along the line of sight. A comparison of the dust temperature distribution with that of the gas temperature (obtained from molecular line measurements) can give important information on the dust-gas coupling in star forming regions. For medium to high mass embedded YSOs, dust is the dominant source of heating of the gas (outside the H II region). A FIR study of an individual star formation complex (at a known distance) can measure the luminosity function above a threshold which can usually be translated to the present day mass function and even initial mass function.

Systematic differences can be expected between star forming regions at different galactocentric distances, since the star formation process depends on the physical conditions of the local ISM (e.g. density, composition, radiation field etc.). This important issue has been addressed by many authors using various techniques. Systematic studies in radio continuum and molecular line emission based on colour selected samples from the IRAS Point Source Catalog (hereafter IRAS PSC) have led to very useful databases which can be the starting point for further studies (Wood & Churchwell 1989a; Wouterloot & Brand 1989).

Although the IRAS mission has proved to be a corner stone in improving our understanding of star formation in the Galaxy, its sub-optimal angular resolution in the 60 and 100 μm bands has been a major limitation. In addition, recent ISO measurements of nearby spiral galaxies have shown the importance of emission at wavelengths > 100 μm and colder dust (T < 25 K) seems to be a dominant constituent of spiral galaxies in general (Alton et al. 1998). This suggests a similar role for colder dust in our Galaxy also.

In view of the above, the TIFR 1-metre balloon borne telescope is flown regularly to map Galactic star forming regions simultaneously in two FIR bands with near diffraction limited angular resolution. These FIR bands have been chosen to be trans-IRAS (λ_{eff} = 148 & 209 μm), so that the distribution of interstellar dust cooler than ≈ 30 K which might have been missed by IRAS, can be traced (Ghosh 2000, Mookerjea et al.
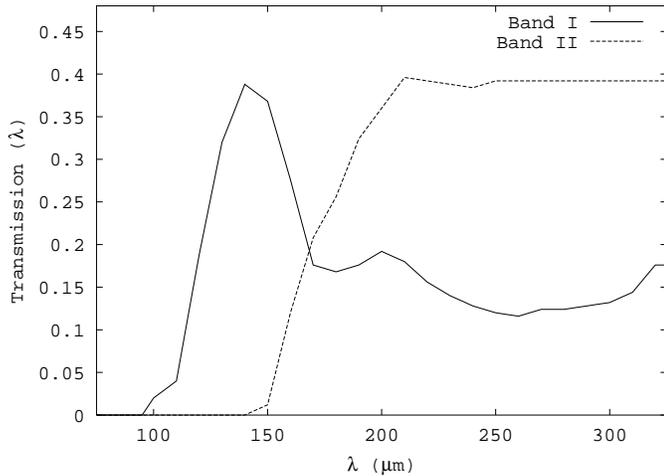
Fig. 1. The relative responses of the two far infrared bands of the photometer used onboard the 1-meter balloon borne TIFR telescope.

1999, 2000a, 2000b). Accessibility of more than 90% of the Galactic plane ($l = 315^0 - 0^0 - 290^0$) from the Indian balloon launching station has been exploited by targeting the southern sky, which is observationally less explored in the FIR.

The catalogue of CO emission associated with colour selected IRAS PSC sources by Wouterloot & Brand (1989; hereafter WB89) covers the longitude range of the Galactic plane of interest to us. Based on information from this catalogue, the star forming complex around IRAS 09002-4732 was selected for the present study because: (i) all the four bright IRAS PSC sources in this region have similar kinematic distances (WB89; Sugitani & Ogura 1994); three of them (IRAS 08589-4714, 09002-4732 and 09014-4736) are known to be physically associated, hence this complex presents an opportunity to derive its PDMF / IMF if a reasonable number of sources are detected; (ii) it lies marginally outside the solar circle, hence a comparison of the physical conditions in this region with that in the 4–5 kpc molecular region and regions inside the solar circle would be interesting; (iii) the complex is very close to the Galactic mid plane with $z \approx 20$ pc (WB89) as compared to the scale height of 90 pc for the embedded OB stars (Wood & Churchwell 1989b). This region around IRAS 09002-4732 is associated with the very extended Vela Molecular Ridge detected in the wide angle survey of ^{12}CO emission by May et al. (1988) and Murphy and May (1991), and more recently mapped by Yamaguchi et al. (1999) in both ^{12}CO and ^{13}CO lines.

Most of the available observational data for this region pertain to IRAS 09002-4732 itself and clearly indicate the presence of an embedded young stellar object in a dense molecular cloud. These include measurements of radio continuum (Caswell & Haynes 1987; Manchester & Goss 1969; Whiteoak 1992; Walsh et al. 1998), infrared spectra from the IRAS Low Resolution Spectrometer Catalog (hereafter LRS; Olnon & Raimond, 1986), ISO Long Wavelength Spectrometer data (ISO-LWS; Clegg et al. 1996) and photometric and imaging measurements in the near and mid infrared (Lenzen 1991; Walsh et al. 1999). In addition, millimeter wave continuum emission

(Reipurth et al. 1996) and molecular line detection of CS have been reported (Zinchenko et al. 1995). A recent multi transitional study of IRAS 09002-4732 has led to the detection of bipolar outflow emission in the CS line with distinct red and blue shifted peaks displaced symmetrically relative to the central IR object (Lapinov et al. 1998). However, no bipolar emission in the CO line has been seen by them.

The observations of a large region (area > 500 sq. arc min) centered at IRAS 09002-4732 are presented here. This Galactic H II region / molecular cloud complex has been studied with the aim of understanding the energetics, physical sizes, spatial distribution of interstellar dust and its temperature. The next section describes the observations and the results alongwith the discussions are presented in Sect. 3.

2. Observations

2.1. Balloon-borne observations

The Galactic star forming region associated with IRAS 09002-4732 was mapped using a new 12 channel two band far infrared (FIR) photometer system at the Cassegrain focus of the TIFR 100 cm (f/8) balloon borne telescope. Details of the 100 cm telescope system and the observational procedure have been described elsewhere (Ghosh et al. 1988; Mookerjea et al. 1999). This 12 channel photometer was flown for the first time on 18 November, 1993 from the TIFR Balloon Facility, Hyderabad (Latitude = 17°.47 N, Longitude = 78°.57 E). A pair of six element (2×3 close packed configuration) composite Silicon bolometer arrays was used as FIR detectors and were cooled to 0.3 K using a closed cycle ^{3}He refrigerator (Verma et al. 1993). The same region of the sky was viewed simultaneously in two FIR bands with near identical fields of view of $1'.6$ per bolometer, thus instantaneously covering an area of $6'.0 \times 3'.4$ in each band. A series of filters and a CsI beam splitter define the two FIR wavebands. The spectral transmission of the total system in each FIR band was determined in the laboratory using a Michelson interferometer and a Golay cell as the reference detector. The resulting transmission curves for the two bands are shown in Fig. 1. Since the configuration of the cryogenically cooled filters which define the FIR pass bands, have been upgraded from time to time, these bands differ from those in Mookerjea et al. (1999).

The sky was chopped along the cross-elevation axis at 10 Hz with a throw of $4'.2$. The relative responses of individual bolometers, absolute flux calibration of the photometer as well as of the instrumental point spread function (PSF) were determined from raster scans across Jupiter. The PSF also includes the effect of the sky chopping. The calculated effective wavelengths and measured sensitivities for the two FIR bands for various relevant grey body spectra of different temperatures are presented in Table 1. Hereafter, the two bands will be referred to as 148 and 209 μm bands corresponding to the λ_{eff} for a 30 K source with λ^{-2} emissivity. The region of the sky $\approx 27' \times 20'$, centered on IRAS 09002-4732 was mapped twice. The mapped region also included the IRAS Point Source Catalog (hereafter PSC) sources IRAS 08583-4719, 08589-4714 and 09014-4736.
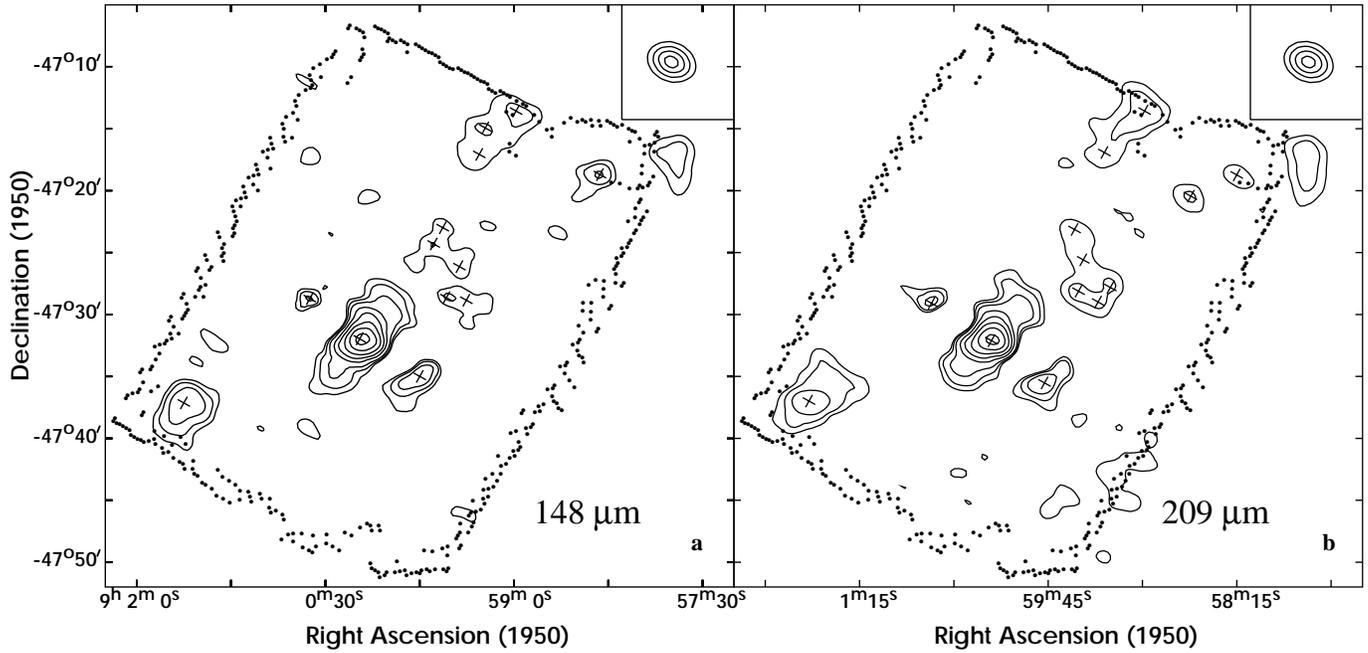
Fig. 2a and b. The intensity maps for the region around IRAS 09002-4732 in TIFR bands – **a** at 148 μm with peak = 3079 Jy/sq. arcmin, **b** at 209 μm with peak = 1611 Jy/sq. arcmin. The isophot contour levels in both **a** and **b** are 80, 40, 20, 10, 5, 2, 1, &.5% of the respective peaks. The crosses mark the positions of sources detected in respective bands (see Sect. 3.1). The insets show deconvolved images of Jupiter in the respective bands. The contours are 60, 20, 5 & 1% of respective peaks, aligned to the instrumental axes for meaningful comparison.

Table 1. Characteristics of the two band FIR photometer.

T	Band-I				Band-II			
	$\epsilon_\lambda \propto \lambda^{-1}$		$\epsilon_\lambda \propto \lambda^{-2}$		$\epsilon_\lambda \propto \lambda^{-1}$		$\epsilon_\lambda \propto \lambda^{-2}$	
(K)	λ_{eff} (μm)	Relative Sensitivity	λ_{eff} (μm)	Relative Sensitivity	λ_{eff} (μm)	Relative Sensitivity	λ_{eff} (μm)	Relative Sensitivity
10	223	0.46	207	0.58	250	0.85	242	0.95
15	186	0.79	172	0.90	233	0.97	225	1.04
20	169	0.93	159	0.99	225	1.00	217	1.04
25	161	0.98	152	1.01	220	1.01	212	1.02
30	156	1.00	148	1.00	217	1.00	209	1.00
35	153	1.00	146	0.99	215	1.00	208	0.99
40	151	1.00	144	0.98	214	1.00	206	0.98

We carried out phase sensitive detection of individual bolometer signal using an on-board signal processing system. The samples from different bolometers were combined during the off-line data processing pipeline which reconstructs the telescope aspect. This uses the relative responses of the bolometers and a geometric model of their locations in the telescope focal plane. The resulting final chopped FIR signals were gridded into a two dimensional sky matrix (elevation × cross elevation) with a cell size of $0\rlap{.}'3 \times 0\rlap{.}'3$. The observed signal map was deconvolved using an indigenously developed procedure based on the Maximum Entropy Method (MEM) similar to that of Gull & Daniell (1978) (see Ghosh et al. 1988, for details). The determination of the absolute aspect of the telescope was improved by using a focal plane optical photometer which detects stars (in an offset field) while the telescope scans the programme source.

An absolute positional accuracy of $\sim 0\rlap{.}'5$ has been achieved in the FIR maps using this method. From the deconvolved maps of Jupiter, the FWHM sizes are found to be $1\rlap{.}'0 \times 1\rlap{.}'4$ and $1\rlap{.}'0 \times 1\rlap{.}'3$ in the 148 and 209 μm bands respectively.

2.2. Data from IRAS and ISO missions

The data from the IRAS survey in the four bands (12, 25, 60 and 100 μm) for the region of the sky mapped by us were HIRES processed (Aumann et al. 1990) at the Infrared Processing and Analysis Center (IPAC[1], Caltech). In the present study, these maps have been used for extracting sources and quantifying interband positional associations and flux densities. They have

---

[1] IPAC is funded by NASA as part of the part of the IRAS extended mission program under contract to JPL.

Table 2. Position and flux density details of the detected sources.

#	RA	Dec	IRAS PSC	Flux Density (Jy)							T^b_{FIR}
	(1950)	(1950)	associations	TIFR		IRAS[a]					
	h m s	o ′ ″		209 μm	148 μm	100 μm	60 μm	25 μm	12 μm		(K)
S1	8 58 15.0	–47 18 44	08583-4719	54	209	1242	1309	233	44		>45
	″	″	″			<1692[c]	<469[c]	34.1[c]	6.8[c]		
S2	8 58 36.9	–47 20 27		70	–	767	–	36	25.3		
S3	8 58 59.0	–47 13 35	08589-4714	142	195	680	365	30.1	15.1		21
	″	″	″			551[c]	200[c]	13.5[c]	2.2[c]		
S4	8 59 13.7	–47 14 57		–	179	459	–	–	10.7		
S5	8 59 15.3	–47 27 50		90	118	–	44	–	3.7		20
S6	8 59 16.6	–47 17 05		83	155	–	110	–	10.9		27
S7	8 59 22.8	–47 28 51		102	144	197	55	–	5.3		21
S8	8 59 26.1	–47 26 08		72	121	–	43	–	–		24
S9	8 59 30.5	–47 28 07		102	111	187	54	–	3.4		18
S10	8 59 32.4	–47 23 08		65	102	53	43	–	–		23
S11	8 59 38.3	–47 24 18		–	134	53	43	–	–		
S12	8 59 45.0	–47 35 00		200	384	111	46	17	6.3		28
S13	9 0 12.1	–47 32 07	09002-4732	4753	9127	14057	13611	2577	203		28
	″	″	″			14707[c]	11877[c]	1962[c]	121[c]		
S14	9 0 40.7	–47 29 06		66	111	–	27	–	–		25
S15	9 1 39.1	–47 37 00	09014-4736	282	607	902	795	100	52		33
	″	″	″			957[c]	621[c]	79.6[c]	30.0[c]		

[a] From HIRES processed maps unless specified otherwise. The flux densities are integrated over a circle of 3′.0 diameter.
[b] Determined using the flux densities in TIFR bands and assuming a grey body spectrum with emissivity $\epsilon_\lambda \propto \lambda^{-2}$.
[c] From IRAS Point Source Catalog.

also been used for generating maps of dust colour temperature and optical depth. Since both IRAS 09002-4732 and 09014-4736 appear in the IRAS Low Resolution Spectrometer catalog, their spectra in the wavelength range 8–22 μm have also been used to construct the respective SEDs. Similarly between 45–195 μm, the data from the Long Wavelength Spectrometer onboard ISO have also been used.

3. Results and discussion

3.1. 148 μm and 209 μm bands

The MEM deconvolved TIFR maps at 148 and 209 μm of the Galactic star forming region associated with IRAS 09002-4732 are presented in Fig. 2 (a & b). The insets show the deconvolved intensity contours for the point-like source (Jupiter), to quantify the achieved angular resolution. The dotted lines in these figures mark the boundary of the region covered by the telescope bore-sight. However the actual observations extend beyond this boundary due to the sky chopping and the effective size of the PSF array. As a result, the intensity maps generated by the MEM deconvolution extend further by 3′.4 along in-scan and 6′ along cross-scan directions. The limits for reliable extraction of discrete sources and structural information in the form of isophot contours have been established by using the data from two independent sets of raster scans. The dynamic range has been found to be $\approx$ 200 for both bands. Several regions of extended emission are seen in both the 148 and the 209 μm maps. A total of 15 sources have been detected, details of which are listed

in Table 2 and positions marked on the maps. The four most prominent peaks are associated with IRAS PSC sources, viz., 08583-4719, 08589-4714, 09002-4732 and 09014-4736. The listed flux densities have been obtained by integrating over a circle of 3′ diameter.

The positions of the global peaks in both the 148 and 209 μm maps are identical to that of IRAS 09002-4732. The direction of the major extended emission seen from IRAS 09002-4732 in both the TIFR maps [size at 10% (50%) of peak: 3′.8 × 2′.9 (1′.8 × 1′.6) at both these bands] matches quite well with mm-wave molecular line maps. The CS (2–1) map of Zinchenko et al. (1995) shows a FWHM size of $\approx$ 2′ × 1′.5 with the major axis at almost identical position angle as the FIR extension. Higher angular resolution map by Lapinov et al. (1998) in the CS (7–6) line resolves the central region into two peaks with different LSR velocities nearly symmetrically displaced relative to the FIR peak. The line joining these two peaks also has a similar position angle.

3.2. IRAS bands

The HIRES processed maps in all the four IRAS bands for the region of present study are shown in Fig. 3 (a,b,c & d). The dynamic range of these HIRES maps is larger than that of the TIFR maps, and the isophots have been shown down to 0.1% of respective peak intensities. Due to this larger dynamic range, the diffuse emission is more prominently visible in these HIRES maps.
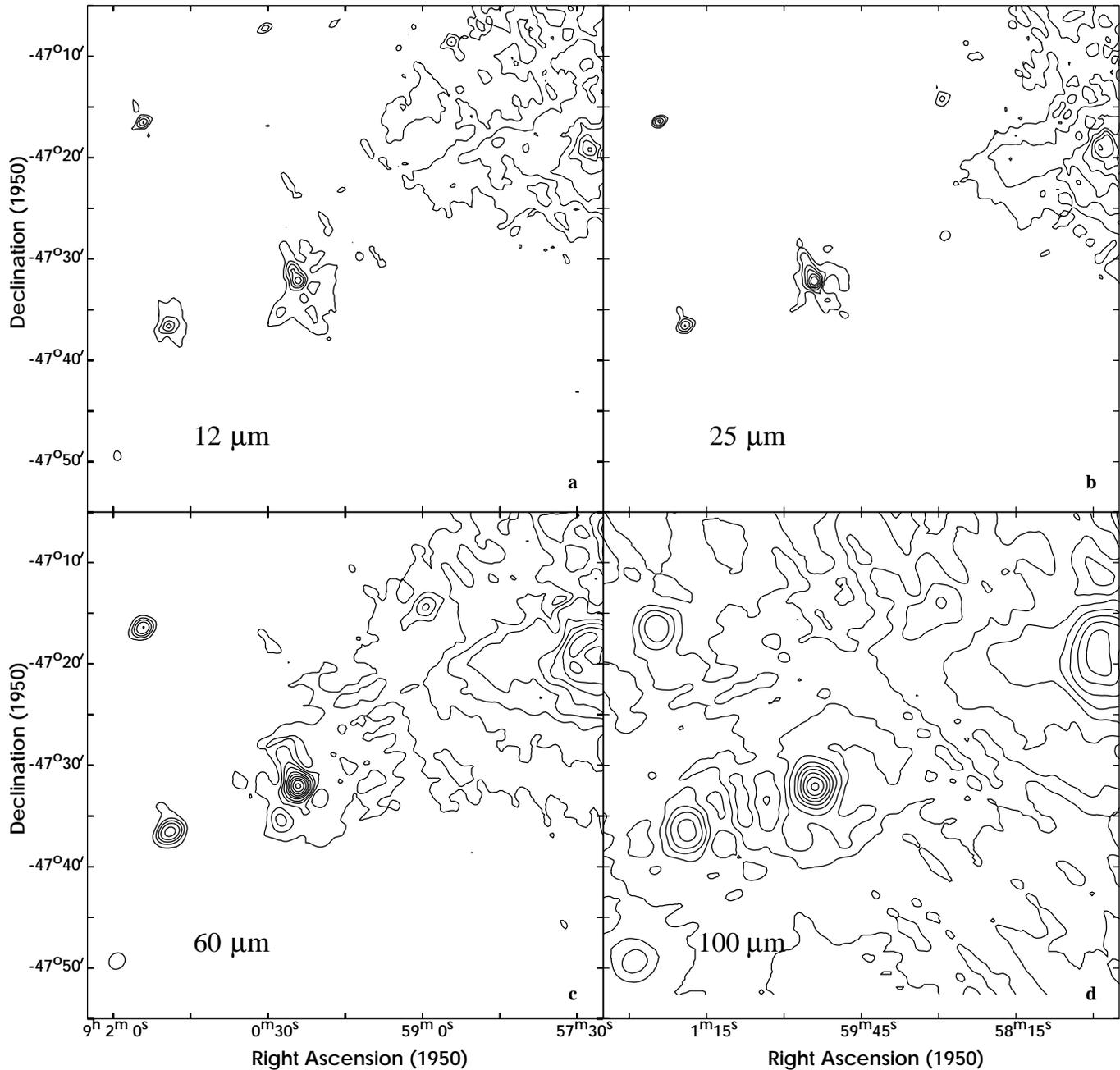
Fig. 3. The HIRES processed IRAS maps for a similar region as shown in Fig. 2, in the four bands – **a** at 12 μm with peak = 374 Jy/sq. arcmin, **b** at 25 μm with peak = 5470 Jy/sq. arcmin. **c** at 60 μm with peak = 12300 Jy/sq. arcmin. **d** at 100 μm with peak = 5830 Jy/sq. arcmin. The isophot contour levels in **a** & **b** are 90, 30, 10, 3, 1,.3, &.1% and in **c** & **d** are 80, 40, 20, 10, 5, 2.5, 1,.5,.25 &.1% of the respective peaks.

The angular resolutions achieved in these maps (in-scan $\times$ cross-scan) are $0.'52 \times 0.'63$, $0.'58 \times 0.'70$, $1.'15 \times 1.'35$ and $1.'87 \times 1.'97$ at 12, 25, 60 and 100 μm respectively.

A new algorithm has been used to extract sources in the HIRES processed IRAS survey maps. The scheme works on the local maxima in the intensity maps as candidates and models the local background (encompassing the source of an assumed size, which is a variable: 1–4$'$) and subtracts the same. The flux densities (3$'$ diameter) for these HIRES sources are also presented in Table 2.

3.3. Discrete sources

Out of the total 15 FIR sources that have been detected from the TIFR maps, 12 are common to both the 209 μm and 148 μm bands (Table 2). All these 15 sources are found to be associated with sources extracted from the HIRES maps in at least one band (13 in at least 2 HIRES bands). The positional match demanded is within $1.'5$ for the purpose of association. Four of these are associated with IRAS PSC sources whose SEDs are studied in greater detail (Sect. 3.6). The IRAS PSC flux densities for these
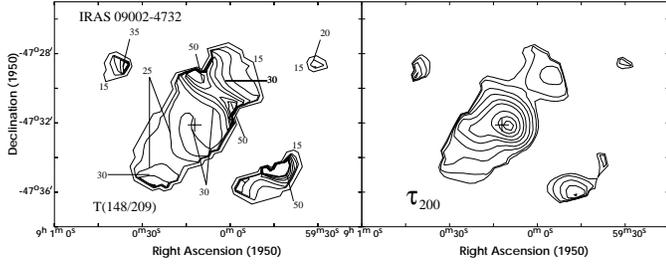
Fig. 4. The distribution of dust temperature T(148/209), and optical depth at 200 μm, τ_{200}, for the region around IRAS 09002-4732 (A) assuming a dust emissivity law of $\epsilon_\lambda \propto \lambda^{-2}$. The isotherms correspond to 15 K to 50 K in steps of 5 K. Temperature values for a few contours are displayed to avoid ambiguity. The τ_{200} contours represent 90, 70, 50, 30, 20, 10, 5, 2 & 1% of the peak value of 0.051. The cross marks the position of IRAS 09002-4732.
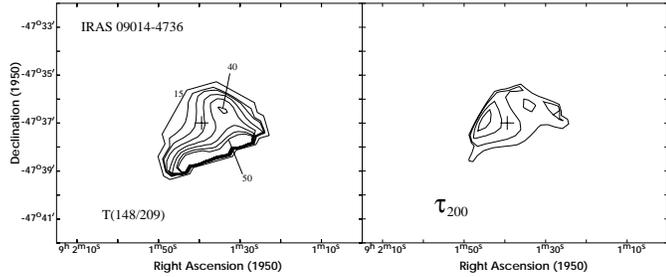

Fig. 5. Same as in Fig. 4, but for the region around IRAS 09014-4736 (B). The isotherms refer to the same temperatures as in Fig. 4. The τ_{200} contours represent 10, 5, 2 & 1% of the global peak value of 0.051. The cross marks the position of the TIFR source (S15) associated with IRAS 09014-4736.

four sources are also listed in Table 2. The dust temperatures in the FIR, T_{FIR}, have been computed from the flux densities in the TIFR bands, assuming an emissivity law of $\epsilon_\lambda \propto \lambda^{-2}$. These are also listed in Table 2.

An attempt has been made to determine γ, the slope of the IMF ($dN/d(logM) \propto M^\gamma$), for the region around IRAS 09002-4732, under reasonable assumptions. We assume all the 15 sources to be nearly at the same distance based on the finding of WB89 (3 out of the 4 IRAS PSC sources in this region for which CO emission has been found, are at distances within $\pm$ 10%). If each source represents one embedded ZAMS star, and their luminosities are translated to stellar masses using Tout et al. (1996), then the local slope of the IMF, γ has been found to be $-1.25^{+0.75}_{-0.65}$ for the mass range 4–16 $M_\odot$. The effect of incompleteness near the sensitivity limit has been avoided by appropriate choice of the mass bins based on the source number distribution. This slope is similar to those found for Galactic OB associations (Massey et al. 1995) and clusters (Phelps & Janes 1993).

3.4. Diffuse emission

Using the T(148/209) temperature distribution for the entire region mapped (Sect. 3.5), and the intensity maps in the same region, the total far-infrared luminosity has been estimated, assuming the dust emissivity law to be $\epsilon_\lambda \propto \lambda^{-2}$. For the regions of the intensity maps with S/N < 3 in either band, a fixed value of 10 K has been assumed for the dust temperature. The contribution of diffuse emission in this complex is found to be ~2.8×10^4 $L_\odot$, which is 35% of the total emission. This does not include contribution from any diffuse (structureless at < 10′) component which may be associated with the Vela Molecular Ridge clouds along the line of sight. This fraction is in agreement with the values found for young Galactic star forming regions, viz., 25% for Orion A region (Mookerjea et al. 2000b); 35% for W 31 complex (Ghosh et al. 1989).

3.5. Distribution of dust temperature and optical depth

Although the HIRES processed IRAS maps have a much higher dynamic range, the angular resolution of the TIFR maps is superior to the IRAS maps at 60 and 100 μm, due to the smaller and circular beams employed. Taking advantage of the nearly identical beams of the TIFR bands at 148 and 209 μm and the simultaneity of observations, we have generated reliable maps of dust temperature and optical depth (at 200 μm, τ_{200}; translated from 209 μm), assuming a dust emissivity of $\epsilon_\lambda \propto \lambda^{-2}$ following the same procedure as described in Mookerjea et al. (1999, 2000b). The dust temperatures are calculated based on the assumption that the dust is optically thin which is reasonable at these wavelengths. Considering the uncertainties in the flux densities measured by us and the wavelength regime probed by us, the temperature computed has an uncertainty of $\sim \pm 2$K, between 15 K and 35 K which gradually increases to ± 5K at 50 K.

Two regions with relatively stronger FIR emission have been selected out of the entire mapped area for presenting the T(148/209) and τ_{200} distribution. These two regions cover the target source IRAS 09002-4732 (hereafter, A) and the neighbouring source IRAS 09014-4736 (B). The spatial distribution of T(148/209) as isotherm contours and contours of constant τ_{200}, for the regions A and B are presented in Figs. 4 and 5 respectively.

The HIRES maps at 60 and 100 μm trace the distribution of somewhat warmer dust (30–50 K). We have used these to generate maps of the colour temperature, $T(60/100)$, and optical depth (τ_{100}) for the region A (around IRAS 09002-4732). The intensity maps at 60 and 100 μm were spatially averaged before computing $T(60/100)$ and τ_{100} in a manner similar to that described by Ghosh et al. (1993) for an emissivity law of $\epsilon_\lambda \propto \lambda^{-1}$. This emissivity law is more appropriate for the 60–100 μm wavelength range. The isotherms of T(60/100) and contours of constant τ_{100} are presented in Fig. 6 (a & b).

The position of the intensity peaks in both the TIFR as well as all four IRAS bands for the region A are identical to that of IRAS PSC coordinates of IRAS 09002-4732, which has been marked on Figs. 4 and 6. It may be noted here that the positions of the associated radio continuum source at 843 MHz (Whiteoak 1992) and H$_2$O maser source are within 15″ of IRAS 09002-4732 (Lapinov et al. 1998).

The T(148/209) temperature distribution is very asymmetrical around IRAS 09002-4732. Hotter dust and a steeper temperature gradient are seen towards the north-west (NW) of IRAS 09002-4732 and a relatively smoother temperature distribution in the range of 20 – 30 K is observed towards the south-east. The band of hotter dust is situated $\sim 2'.2$ to the NW of the peak position of the FIR intensity. The dust temperature drops from a value of ~ 50 K to 20 K within a distance of ≈ 0.8 pc. Similar large variations in dust temperature have been seen for the regions associated with IRAS 00494+5617 and IRAS 05327-0457 (Mookerjea et al. 2000a).

The T(60/100) map shows one major peak, coinciding with the position of IRAS 09002-4732 and the temperature drops (to 25 K) on all sides almost symmetrically except for the region to the north. The values of T(60/100) would come closer to T(148/209), if the dust emissivity exponent is chosen to be -2 (see Fig. 6 caption). The lack of complex structure in this T(60/100) map vis-a-vis T(148/209) map may be due to the poorer angular resolution of the IRAS maps.

The distribution of optical depth (τ_{200}) around IRAS 09002-4732, somewhat resembles the intensity distribution: the peak position matches with that of I_{148} or I_{209}. The peak τ_{200} value is 0.051. There is a secondary peak in this map shifted towards the NW (beyond the band of higher temperature), positionally matching with relatively cooler dust [T(148/209) $\sim 20 - 25$ K].

The τ_{100} distribution is similar to that of τ_{200} only near the peak of the intensity maps. This may not be surprising, since the IRAS and TIFR maps are probing dust column densities at different temperatures. The highest value of τ_{100} occurs $\sim 2'$ south-west of IRAS 09002-4732. The value of τ_{100} near the peak of the intensity maps, is 0.023.

The T(148/209) temperature distribution in IRAS 09014-4736 also shows asymmetric structures (Fig. 5a). A ridge of hot dust runs approximately east-west $\sim 1'.5$ away (south) from the peak of FIR intensity distribution. In addition, a local hotspot is seen due north-west ($1'.2$) from the intensity peak. The τ_{200} distribution shows one major peak positionally corresponding to ~ 20 K dust, and an isolated minor peak at the position of the hotspot.

3.6. Radiative transfer modelling

With the aim of extracting important physical parameters, an attempt has been made to construct radiative transfer models for the four IRAS PSC sources IRAS 09002-4732, 09014-4736, 08583-4719 and 08589-4714, which have been covered in our FIR maps. The self consistent scheme developed by Mookerjea & Ghosh (1999) has been used for this purpose which is briefly described below. This scheme models spherically symmetric cloud with centrally embedded young stellar object/(s), immersed in an average interstellar radiation field. Although the gas-dust coupling is not considered explicitly, the role of the gas in the energetics of the cloud has been included in a self consistent manner. Two commonly used types of interstellar dust have been explored (Draine & Lee 1984, hereafter DL; Mezger et al. 1982, hereafter MMP), with a power law size distribution
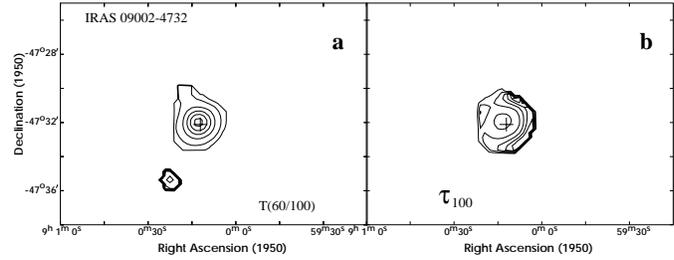

Fig. 6a and b. The **a** dust temperature T(60/100) and **b** optical depth at 100 μm (τ_{100}) distribution from the HIRES maps for the region around IRAS 09002-4732 (A) assuming a dust emissivity law of $\epsilon_\lambda \propto \lambda^{-1}$. The isotherms displayed in **a** correspond to the temperatures 70, 60, 50, 40, 30 & 25 K. The innermost contour is for the hottest dust (70 K). (The isotherms would represent 50, 45, 39, 33, 26 & 22 K if the emissivity index was -2). The contours in the optical depth map **b** represent 50, 40, 30, 20 & 10% of the global peak value of 0.11. The cross marks the position of IRAS 09002-4732.

given by Mathis et al. (1977). For each type of dust, the relative proportion of graphite and astronomical silicate grains is selectable. The observational constraints include the SED due to the dust, angular sizes at different wavelengths and the radio continuum emission.

The following parameters are explored in order to get an acceptable fit to all the data: (i) the nature of the embedded source, which could either be a single ZAMS star or a cluster of ZAMS stars consistent with the Salpeter Initial Mass Function; (ii) radial density distribution law (only three power laws have been explored, viz., $n(r) \propto r^\alpha$, with $\alpha = 0, -1$ or -2); (iii) the relative abundances of the two constituent grain types; (iv) total radial optical depth due to the dust (inclusive of all constituents) at a selected wavelength (τ_{100} at 100μm); (v) the gas to dust ratio by mass (the predicted radio continuum emission is sensitive to this); (vi) geometric details of the dust cloud (e.g. cavity size, outer size of the cloud).

The distances to all the four IRAS PSC sources in the present study, have been taken to be 1.4 kpc.

3.6.1. IRAS 09002-4732

The observed SED of IRAS 09002-4732 has been constructed using TIFR, IRAS-HIRES, IRAS-LRS and ISO-LWS data (Fig. 7a). In addition, 1.3 mm continuum measurement of Reipurth et al. (1996) and near infrared data from Lenzen (1991) have been used. The total radio continuum emission has been found to be 3.8 Jy at 5 GHz (Caswell & Haynes 1987) from this source in a wide beam ($4'.4$). Whiteoak (1992) found the flux density at 843 MHz to be 2.1 Jy. Recent high angular resolution (synthesized beam $\approx 2''$) measurement for the central region by Walsh et al. (1998) at 8.64 GHz, gives a peak intensity of 0.5 Jy/beam. The total luminosity and the rate of Lyman continuum photon generation has been estimated to be $6.9 \times 10^4 L_\odot$ and 7.1×10^{47} s^{-1} respectively by Simpson & Rubin (1990). By integrating the observed SED, we estimate the total luminosity to be $1 \times 10^5 L_\odot$. In a study of a sample of ultracompact H II
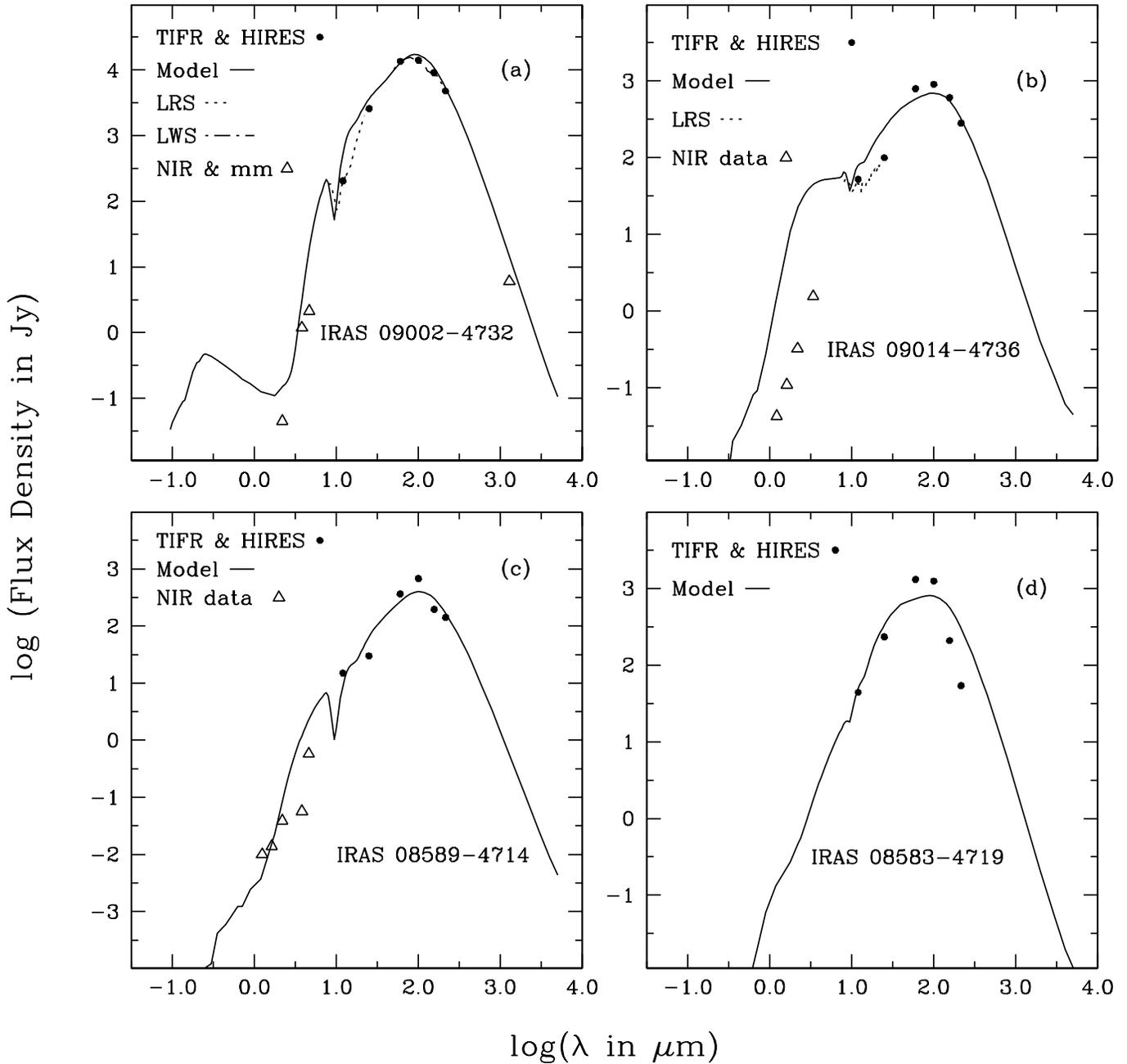
Fig. 7. Comparison of the predicted spectral energy distributions (SEDs) from the best fit models of **a** IRAS 09002-4732, **b** IRAS 09014-4736 **c** IRAS 08583-4719 & **d** IRAS 08589-4714 with observations. The filled circles represent the TIFR and IRAS-HIRES data. The dashed lines are IRAS-LRS spectra (for IRAS 09002-4732 and IRAS 09014-4736) and the dash dot line is the ISO-LWS spectrum of IRAS 09002-4732. The triangles denote 1.3 mm data from Reipurth et al. (1996) for IRAS 09002-4732 and near-IR data from Lenzen (1991) for IRAS 09002-4732, from Persson & Campbell (1987) for IRAS 09014-4736, from Lorenzetti et al. (1993) for IRAS 08589-4714. The solid line denotes the prediction of the best fit model. See text and Table 3 for details of the model parameters.

regions which includes IRAS 09002-4732, Walsh et al. (1999) have fitted the infrared part of the SED by representing it as a two-component black body spectrum and also by a radiative transfer model. Our self consistent modelling scheme includes angular sizes at different wavelengths, radio continuum data as well as dust composition and grain size distribution.

The best radiative transfer model for IRAS 09002-4732 has been identified by varying the parameters and comparing the following predictions with observations: (i) the SED originating from the dust, (ii) the angular sizes at different wavebands, and (iii) the radio continuum emission from the gas component. The predicted angular sizes have been convolved with the relevant

Table 3. Parameters for the best fit radiative transfer models.

Source	α	R_{max} (pc)	R_{min} (pc)	r_{HII} (pc)	τ_{100}	Luminosity ($10^3 L_\odot$)	Dust composition[a] Silicate:Graphite	M_{dust} ($M_\odot$)
IRAS 08583-4719	0.0	0.3	5.0×10^{-5}	2.9×10^{-3}	0.02	4.0	81: 19	0.50
IRAS 08589-4714	0.0	0.2	8.0×10^{-5}	1.2×10^{-3}	0.05	2.4	81: 19	0.55
IRAS 09002-4732	0.0	1.0	3.0×10^{-2}	5.5×10^{-2}	0.05	100	72: 28	14
IRAS 09014-4736	-1.0	0.8	8.0×10^{-5}	2.9×10^{-5}	0.03	6.5	81: 19	0.80

[a]Dust is of DL type for all the four sources.

telescope beams, prior to comparison with observed FWHM sizes. The embedded source is found to be a single ZAMS O7 star with $N_{Lyc} = 3.6 \times 10^{48}$ s^{-1} and $T_{eff} = 38{,}500$ K. The preferred type of dust is DL and the density distribution is uniform. The gas to dust ratio is 100: 1 by mass. The other parameters of the best fit model for IRAS 09002-4732 are presented in Table 3.

The predicted SED from this model is compared with the observations in Fig. 7 (a). The model fits the data quite well. The predicted total radio continuum emissions (1.5 Jy at 843 MHz; 3.7 Jy at 5 GHz & 3.5 Jy at 8.6 GHz) are also in reasonable agreement with observations. For our model, the H II region extends into the dust cloud beyond the dust-free central cavity ($r_{HII} > R_{min}$), and its size is of similar order as inferred from the 8.6 GHz map by Walsh et al. (1998). A comparison of the predicted angular sizes at mid to far infrared wavelengths with the measurements is presented in Table 4. The predicted angular sizes increase as a function of the wavelength and the values are in general agreement within errors.

The IRAS LRS catalog has classified IRAS 09002-4732 to be of type 81 based on the strengths of emission of the unidentified 11.3 μm feature and the [Ne II] line at 12.8 μm. Our inference of an embedded O7 star from the above modelling is consistent with the detection of the [Ne II] line. However, the detection of 11.3 μm feature, generally attributed to be arising from single photon absorption processes of PAH molecules, indicates importance of non-equilibrium heating processes, which is beyond the scope of the present study.

The total mass of our model cloud is 1400 $M_\odot$ (gas to dust ratio = 100) which can be compared with inferences from molecular line observations. The virial mass estimate from the CO data of WB89 and using the relation of Evans (1999; see Eq. 8), we get the cloud mass to be 1710 $M_\odot$ which is reasonably close to the mass from our model considering the uncertainties. On the other hand, the mass estimate from CS line measurements is 607 $M_\odot$ (Zinchenko et al. 1995). The (L/M) ratio of the total IR luminosity to cloud mass from the model, the virial mass based on CO data, and the CS core mass, are 71, 58 and 165 $L_\odot/M_\odot$ respectively, for IRAS 09002-4732.

3.6.2. IRAS 09014-4736

The FIR emission from IRAS 09014-4736 at 148 and 209 μm is quite extended as evident from Fig. 2 and it is listed in the IRAS Small Scale Structure Catalog (SSSC; X0901-476) due to its extended emission in 25 and 60 μm bands. It is gratifying to

Table 4. Comparison of predicted sizes from the best fit model for IRAS 09002-4732 with observed FWHMs.

Wavelength (μm)	Model ($'$)	Observations ($'$)
12	0.59	0.54
25	0.61	0.62
60	1.07	0.89
100	1.96	1.33
148	2.4	1.8
209	2.5	1.8

note that the flux densities listed in the SSSC (109 Jy at 25 μm and 794 Jy at 60 μm) match extremely well with flux densities (100 and 795 Jy respectively; see S15 in Table 2) determined using our source extraction scheme from the HIRES processed maps (Sect. 3.2). The angular sizes estimated in SSSC are: $1'$ at 25 μm and 1.6 at 60 μm. The FWHM sizes (major $\times$ minor) in the 148 and 209 μm bands are 3.5×2.7 and 3.8×2.5 respectively. The size increases with wavelength as expected.

The observed SED for IRAS 09014-4736 has been compiled using the TIFR, IRAS-HIRES and IRAS-LRS data (Fig. 7b). No radio continuum data for this source are available in the literature. However, this region has been covered by the 843 MHz survey with $43''$ angular resolution (Whiteoak 1992). The quoted completeness limit of 50 mJy by Whiteoak (1992) has been used here as an upper limit. Modelling the SED of IRAS 09014-4736 leads to a better fit for an r^{-1} density distribution law than for an r^0 law. The embedded source is found to be a ZAMS star of B1 type ($T_{eff} = 22{,}600$ K). The preferred dust is of DL type with the radial optical depth, $\tau_{100} = 0.03$. The other parameters corresponding to the best fit model for IRAS 09014-4736 are listed in Table 3. The spectral fit of this model to the observed SED is displayed in Fig. 7 (b) which is reasonably good. There is hardly any detectable radio continuum emission as expected for a B1 type star.

Near and mid-IR spectrophotometry of IRAS 09014-4736 shows recombination line emission of hydrogen (Persson & Campbell 1987; Beck et al. 1991; Porter et al. 1998). The LRS spectrum of this source has been classified as type 80 based on the detection of 11.3 μm feature and absence of any fine structure line from ionized heavier elements, typical of low excitation H II region. Detection of several additional PAH features (Cohen et al. 1989; de Muizon et al. 1990; Zavagno et al. 1992) further supports that IRAS 09014-4736 has an embedded YSO. Al-

though IRAS 09014-4736 is classified as an unidentified source in the IRAS PSC, it is situated within $\approx 20''$ of the small optical nebula, BBW 225 (size $< 2'$), identified by Brand et al. (1986). The embedded YSO (B1) inferred from our modelling is consistent with all of the above. However, the actual geometry of the source has to be far from spherically symmetric, in order to reconcile with the size of the optical nebula and the near infrared data. Similar conclusions have been arrived at by Beck et al. (1991) for IRAS 09014-4736.

The only available molecular line observation from this source is the CO emission (WB89). We estimate the molecular gas density and the virial mass for the cloud associated with IRAS 09014-4736 to be 5.2×10^3 cm^{-3} and 395 $M_\odot$ respectively. The mass of the model cloud is 80 $M_\odot$ for a gas to dust mass ratio of 100. The latter is not constrained well due to the lack of radio continuum emission. The (L/M) ratio corresponding to the model and the virial mass of this cloud are 81 and 16 $L_\odot/M_\odot$ respectively.

3.6.3. IRAS 08589-4714

In addition to the measurements presented here, the near-IR data of Lorenzetti et al. (1993) have been used to construct the SED of IRAS 08589-4714 (Fig. 7c). The parameters of the best fit radiative transfer model are presented in Table 3. A constant density cloud with DL type dust grains is implied. The total radial $\tau_{100} = 0.05$ and the model cloud mass is 55 $M_\odot$. Since the energizing stellar source is detectable in the near-IR, this is an example of very evolved stage of star formation, where only a small fraction of the original interstellar matter is left around the star at present.

The source IRAS 08589-4714 has been detected in CO and CS surveys by Wouterloot & Brand (1989) and Bronfman et al. (1996) respectively. Whereas our model gives a value for the L/M ratio to be ≈ 44 $L_\odot/M_\odot$, the virial mass of the cloud estimated from the CO data of WB89 indicates a value of 3.7 $L_\odot/M_\odot$.

3.6.4. IRAS 08583-4719

IRAS 08583-4719 is contained in the catalog of bright rimmed clouds which are candidates for star formation by radiation driven implosion (Sugitani & Ogura 1994). Unfortunately no additional observational data pertaining to a SED are available other than those presented here. The physical size estimate has been taken from Sugitani & Ogura (1994). Once again a constant density dust (DL) cloud gives the best fit to the SED (Fig. 7d). However, the fit to the observations even for this best model is not very satisfactory. The parameters for this model are listed in Table 3. The mass of the model cloud is 50 $M_\odot$ leading to a (L/M) ratio of 80 $L_\odot/M_\odot$.

3.6.5. Inferences from the modelling

The DL type of dust is favoured for all the four sources modelled here. It may be noted that the emissivity index in the $100-$ 200 μm range for DL type dust (for both silicate and graphite), is $\approx$ -2, consistent with our choice for generation of T(148/209) maps (Sect. 3.5). Three of these four sources suggest a constant density dust envelopes around the YSOs. This conclusion seems to be very common for several Galactic star forming regions: e.g. for IRAS 18314-0720, 18355-0532 and 18316-0602 (Mookerjea & Ghosh, 1999); IRAS 00338+6312, 04004-5114 and RAFGL 5111 (Mookerjea et al. 1999); IRAS 00494+5617 and 05327-0457 (Mookerjea et al. 2000a). The following comments can be made by comparing the parameters for the four sources modelled here: The dust cloud corresponding to IRAS 09002-4732 has the largest size of the central cavity, which contains the most luminous embedded source. Except IRAS 09014-4736, for all other three sources, the H II regions extend well into the respective dust clouds. This emphasizes the role of dust grains on the emission of recombination lines and radio continuum. The radial optical depth due to the dust ranges between 0.02 to 0.05 which is slightly on the lower side compared to IRAS 00494+5617 (Mookerjea et al. 2000a), 00338+6312 (Mookerjea et al. 1999). The interstellar dust composition is found to be nearly identical in all the four sources modelled, viz., Silicate dominated. The ratio between the graphite and the silicate grains, in general vary drastically among the Galactic star forming regions (Mookerjea et al. 1999, 2000a). Hence, nearly identical dust composition found here further supports the hypothesis that the entire complex around IRAS 09002-4732 mapped by us is physically associated.

The L/M ratio for the four sources studied here, as found from our radiative transfer modelling, falls in a narrow range of $44-81$ $L_\odot/M_\odot$. For three of these for which CO measurements are available, this ratio based on virial masses, fall in somewhat broader range ($3.7-58$ $L_\odot/M_\odot$). These can be compared with the results from other studies: (i) A study similar to the present one, for the W 31 complex has lead to a value of (L/M) in the range of $1.6-3.6$ $L_\odot/M_\odot$ (Ghosh et al. 1989); (ii) the average value for a large sample of clouds using virial mass based on CO measurements, is ~ 4 $L_\odot/M_\odot$ with a spread exceeding a factor of 100 (Mooney & Solomon 1988, Evans 1991); (iii) for denser cores studied in CS emission (Plume et al. 1997) give ~ 190 $L_\odot/M_\odot$ with a spread of a factor of 15. Considering the uncertainties arising due to the fact that the different tracers are sampling different components of the ISM (at possibly different spatial scales), the star forming complex associated with IRAS 09002-4732 can be termed as typical of the Galaxy.

4. Summary

The Galactic star forming region associated with the IRAS source 09002-4732 and its neighbouring region (≈ 0.15 sq. deg.) has been mapped in two far infrared bands at 148 and 209 μm with an angular resolution of $\sim 1'$. A total of 15 sources have been detected including 4 IRAS PSC sources. Several of these are well resolved in both these bands. Diffuse emission contributes 35% of the total FIR emission at 209 μm. Taking advantage of simultaneous observations using identical beams in these two bands, reliable maps of dust colour tempera-

ture [T(148/209)] and optical depth (τ_{200}) have been generated which show many structures. Under reasonable assumptions, the IMF slope for this region has been found to be $-1.25^{+0.75}_{-0.65}$ for the mass range of 4–16 $M_\odot$.

The HIRES processed IRAS survey data for the same region at 12, 25, 60 and 100 μm have also been used for comparison as well as extracting discrete sources positionally matching with those detected at 148 and 209 μm. The spatial distribution of T(60/100) and τ_{100} have also been generated for the region locally around IRAS 09002-4732 for comparison.

Self consistent radiative transfer calculations have been carried out for IRAS 09002-4732, 09014-4736, 08583-4719 and 08589-4714 through spherical dust-gas clouds. The observed infrared sub-mm SED, angular sizes and the radio continuum data have been used to constrain the parameters of the models. Whereas for IRAS 09014-4736 an r^{-1} radial density distribution law is preferred, all the other three sources favour an r^0 law. The geometrical details of the dust-gas clouds, the dust compositions and optical depth, etc. have been quantified by these models. The luminosity per unit mass for these sources lies in a rather narrow range of 44–81 $L_\odot/M_\odot$.

References

Alton P.B., Trewhella M., Davies J.I., et al., 1998, A&A 335, 807
Aumann H.H., Fowler J.W., Melnyk M., 1990, AJ 99, 1674
Beck S.C., Fischer J., Smith H.A., 1991, ApJ 383, 336
Brand J., Blitz L., Wouterloot J.G.A., 1986, A&AS 65, 537
Bronfman L., Nyman L.A., May J., 1996, A&AS 115, 81
Caswell J.L., Haynes R.F., 1987, A&A 171, 261
Clegg P.E., Ade P.A.R., Armand C., et al., 1996, A&A 315, L38
Cohen M., Tielens A.G.G.M., Bregman J., et al., 1989, ApJ 341, 246
de Muizon M.J., Cox P., Lequeux J., 1990, A&AS 83, 337
Draine B.T., Lee H.M., 1984, ApJ 285, 89
Evans N.J., 1991, In: Lambert D.L. (ed.) Frontiers of Stellar Evolution. ASP vol. 20, p. 45
Evans N.J., 1999, ARA&A 37, 311

Ghosh S.K., 2000, Bull. Astron. Soc. of India 28, 225
Ghosh S.K., Iyengar K.V.K., Rengarajan T.N., et al., 1988, ApJ 330, 928
Ghosh S.K., Iyengar K.V.K., Rengarajan T.N., et al., 1989, ApJ 347, 338
Ghosh S.K., Verma R.P., Rengarajan T.N., Das B., Saraiya H.T., 1993, ApJS 86, 401
Gull S.F., Daniell G.J., 1978, Nat 272, 686
Lapinov A.V., Schilke P., Juvela M., Zinchenko I., 1998, A&A 336, 1007
Lenzen R., 1991, A&A 244, 477
Lorenzetti D., Spinoglio L., Liseau R., 1993, A&A 275, 489
Manchester B.A., Goss W.M., 1969, Aust. J. Phys. Astrophys. Suppl. 11, 35
Massey P., Johnson K.E., DeGioia-Eastwood K., 1995, ApJ 454, 151
Mathis J.S., Rumpl W., Nordsieck K.H., 1977, ApJ 217, 425
May J., Murphy D.C., Thaddeus P., 1988, A&AS 73, 51
Mezger P. G., Mathis J.S., Panagia N., 1982, A&A 105, 327
Mookerjea B., Ghosh S.K., 1999, JA&A 20, 1
Mookerjea B., Ghosh S.K., Karnik A.D., et al., 1999, ApJ 522, 285
Mookerjea B., Ghosh S.K., Rengarajan T.N., Tandon S.N., Verma R.P., 2000a, ApJ 539, 775
Mookerjea B., Ghosh S.K., Rengarajan T.N., Tandon S.N., Verma R.P., 2000b, AJ 120, 1954
Mooney T.J., Solomon P.M., 1988, ApJ 334, L51
Murphy D.C., May J., 1991, A&A 247, 202
Olnon F.M., Raimond E., 1986, A&AS 65, 607
Persson S.E., Campbell B., 1987, AJ 94, 416
Phelps R.L., Janes K.A., 1993, AJ 106, 1870
Plume R., Jaffe D.T., Evans N.J., Martin-Pintado J., Gomez-Gonzalez J., 1997, ApJ 476, 730
Porter J.M., Drew J.E., Lumsden S.L., 1998, A&A 332, 999
Reipurth B., Nyman L.A., Chini R., 1996, A&A 314, 258
Simpson J.P., Rubin R.H., 1990, ApJ 354, 165
Sugitani K., Ogura K., 1994, ApJS 92, 163
Tout C.A., Pols O.R., Eggleton P.P., Han Z., 1996, MNRAS 281, 257
Verma R.P., Rengarajan T.N., Ghosh S.K., 1993, Bull. Astron. Soc. of India 21, 489
Walsh A.J., Burton M.G., Hyland A.R., Robinson G., 1998, MNRAS 301, 640
Walsh A.J., Burton M.G., Hyland A.R., Robinson G., 1999, MNRAS 309, 905
Whiteoak J.B.Z., 1992, A&A 262, 251
Wood D.O.S., Churchwell E., 1989a, ApJS 69, 831
Wood D.O.S., Churchwell E., 1989b, ApJ 340, 265
Wouterloot J.G.A., Brand J., 1989, A&AS 80, 149 (WB89)
Yamaguchi N., Mizuno N., Saito H., et al., 1999, PASJ 51, 775
Zavagno A., Cox P., Baluteau J.P., 1992, A&A 259, 241
Zinchenko I., Mattila K., Toriseva M., 1995, A&AS 111, 95